Role of dilution on the electronic structure and magnetic ordering of spinel cobaltites

Sayandeep Ghosh,[1] Sobhit Singh,[2] Deep Chandra Joshi,[1] Prativa Pramanik,[1] Subhradip Ghosh,[1]
Pankaj Kumar Mishra,[1] and Subhash Thota[1,*]

[1]*Department of Physics, Indian Institute of Technology Guwahati, Assam, India, 781039*
[2]*Department of Physics and Astronomy, West Virginia University, Morgantown, West Virginia 26506, USA*

By means of the *first-principles* density functional theory (DFT + U) calculations and experiments, we investigate the role of dilution on the structural, magnetic, electronic, and optical properties of the antiferromagnetic (AFM) spinel Co_3O_4 having Néel temperature (T_N) ~ 30 K. As the octahedral cobalt site of spinel lattice is diluted with Ge, Al, Ti, Ru, and Sn cations, we observe a substantial increase in the size of the unit cell as well as destruction of the long-range magnetic ordering with a spin-orbit compensation effect. The ferrimagnetic ordering in diluted inverse spinels such as $Co_2\Sigma O_4$ (Σ = Ti and Sn) emerges due to the difference in the magnetic moments of two sublattices A (3.87 μ_B) and B (4.16 μ_B for Co_2SnO_4 and 5.19 μ_B for Co_2TiO_4). Experiments and DFT calculations indicate antiferromagnetic configuration for Co_3O_4, Co_2AlO_4 ($T_N \sim 4.8$ K) spinels with an equal and opposite moment of ~ 2.60 μ_B in tetrahedral sites of divalent Co ions and negligible contribution from trivalent B-site Co due to the complete filling of t_{2g} levels having a giant crystal field of ~ 2.5 and 1.8 eV, respectively. However, in Co_2GeO_4 ($T_N \sim 20.4$ K) case AFM behavior originates due to the opposite spins at octahedral sites of divalent Co ions. The remaining spinels Co_2TiO_4 ($T_N \sim 47.8$ K), Co_2RuO_4 ($T_N \sim 16$ K), and Co_2SnO_4 ($T_N \sim 41$ K) are more favorable to ferrimagnetic structure as evident from our magnetization measurements with a different temperature dependence of magnetic moments A(T) and B(T) at tetrahedral A and octahedral B sites, respectively. The variation in the energy band gap ($E_g = 1.68 \rightarrow 3.28$ eV for $Co_2RuO_4 \rightarrow Co_2GeO_4$) obtained from DFT + U calculations are in good agreement with our experimental results ($E_g = 1.52 \rightarrow 3.16$ eV) obtained from the diffusive reflectance spectroscopy. The extent of exchange splitting $\Delta_{EX}^{e_g}$ of tetrahedral Co^{2+} varies between 1.8 and 1.3 eV for Co_3O_4 and Co_2AlO_4, respectively. However, $\Delta_{EX}^{t_{2g}}$ exhibits a decreasing trend (5.2 $\rightarrow$ 3.6 eV for $Co_3O_4 \rightarrow Co_2SnO_4$) with increasing the lattice parameter, except for cobalt-orthogermanate Co_2GeO_4.

I. INTRODUCTION

Spinel cobaltites such as Co_3O_4, Co_2GeO_4, Co_2AlO_4, Co_2TiO_4, Co_2RuO_4, and Co_2SnO_4 are considered as important compounds because of their excellent catalytic activity and potential applications in renewable energy [1–8]. The parent compound Co_3O_4 crystallizes into normal cubic spinel ($AB_2O_4 = (Co^{2+})_A[Co^{3+}, Co^{3+}]_BO_4$) structure in which tetrahedral A sites are occupied by the divalent cobalt, whereas the octahedral B sites are filled with trivalent cobalt ions. Owing to such specific structure this compound exhibits the antiferromagnetic ordering [$\downarrow \mu(Co^{2+})_A + \uparrow \mu(Co^{2+})_A$] with Néel temperature T_N at 30 K which makes it an ideal candidate to study the strong A-B and weak A-A two sublattice antiferromagnetic exchange interactions [6,9,10]. Substitution of nonmagnetic elements (Ge, Al, Ti, Ru, or Sn) at octahedral B sites in Co_3O_4 perturbs the antiferromagnetic (AFM) ordering resulting in ferrimagnetic (FiM) behavior with imbalanced moments on A and B sites in the inverted spinel configuration, e.g., $Co_2\Sigma O_4$ where Σ = Ti, Ru, and Sn [11–15]. In addition to the FiM state, these compounds also display low-temperature insulating spin-glass behavior

($\leqslant 16$ K for Co_2RuO_4) [16]. Among the family of such inverse spinel cobaltites, cobalt-orthogermanate (Co_2GeO_4), orthotitanate (Co_2TiO_4), orthoruthanate (Co_2RuO_4), and cobalt-orthostannate (Co_2SnO_4) are the archetypal systems, where the disorderedness plays an important role in the electronic and magnetic properties [11–15]. In this study we report density functional theory (DFT) based *first-principles* calculations of the aforementioned compounds with a special emphasis on their structural, electronic, and magnetic properties, which are complemented with our experimental observations.

The low-temperature magnetic ordering in Co_2GeO_4, Co_2TiO_4, Co_2RuO_4, and Co_2SnO_4 has been the main focus in recent years where the longitudinal ferrimagnetism and transverse spin-glass components coexist leading to some exotic properties such as bipolar exchange bias ($H_{EB} \sim -20$ kOe at 10 K) and spin-liquid state (< 20 K) [16,17]. In recent years a significant advancement in the characterization techniques has enabled researchers to reinvestigate the magnetic structure of these compounds with high precision. In particular, the competing local intersublattice interactions lead to FiM state with Néel temperature $T_N \sim 41$, 47.8, and 16 K and spin-glass freezing temperature $T_F \sim 39$, 41.5, and 16 K for Co_2SnO_4, Co_2TiO_4 and Co_2RuO_4, respectively [15–19]. At a first glance both compounds Co_2SnO_4 and

*subhasht@iitg.ac.in

235119-1

Co_2TiO_4 look identical (lattice parameter $a_{Co_2SnO_4} = 8.66$ Å, $> a_{Co_2TiO_4} = 8.45$ Å), presumably ferrimagnetism due to imbalance in the magnetic moments of divalent Co ions at tetrahedral [$\mu(A) = 3.87$ $\mu_{B-Co_2SnO_4}$ and 3.87 $\mu_{B-Co_2TiO_4}$] and octahedral sites [$\mu(B) = 4.16$ $\mu_{B-Co_2SnO_4}$ and 5.19 $\mu_{B-Co_2TiO_4}$]. However, Co_2TiO_4 exhibits distinct FiM magnetic ordering and electronic structure below T_N as compared to the Co_2SnO_4. In particular, Co_2TiO_4 shows (i) compensation effect at T_{COMP} (~ 32 K) where the bulk magnetization of two sublattices balance each other, (ii) dissimilar electronic structure $(Co^{2+})[Co^{3+}Ti^{3+}]O_4$ as compared to the $(Co^{2+})[Co^{2+}Sn^{4+}]O_4$, and (iii) dominance of negative magnetization at low temperatures [17,18]. On the other hand, a detailed neutron diffraction study of Co_2TiO_4 and Co_2SnO_4 suggests the presence of intense magnetic reflection $(111)_M$ due to ferrimagnetic ordering; nevertheless, the presence of weak antiferromagnetic coupling leads to an additional low intensity magnetic reflection $(200)_M$ in both compounds [20]. Mandrus *et al.* considered the electronic structure of Co_2RuO_4 as $(Co^{2+})[Co^{3+}Ru^{3+}]O_4$ and observed spin-glass freezing temperature at 16 K [16]. Subsequently, incorporation of Zn at tetrahedral A site leads to extremely weak exchange interactions between the octahedral Ru^{3+} ions without any specific magnetic transition [16].

Antic *et al.* reported that the long-range order diminishes as Li substitutes Ti in Co_2TiO_4. For moderate Li doping spin-glass behavior ensues freezing temperature $T_F \sim 17$ K which follows Vogel-Fulcher law with activation energy $E_a \sim 92$ K at the attempt frequency $f_0 \sim 26$ GHz [21]. However, higher dilution ($x \geqslant 0.5$) results in a change in crystal structure from space group $Fd\text{–}3m$ to $P4_332$, without having much change in the magnetic state [21]. Strooper *et al.* demonstrated that dilution with Ge and Zn in Co_2TiO_4 leads to a drastic decrease of the T_N from 47.8 to 21.5 K and 26 K for Co_2GeO_4 and Co_2ZnO_4, respectively [22,23].

Numerical simulations play an important role in understanding the structural and magnetic behavior of these compounds. In particular, the first-principles *ab initio* based density functional theory (DFT) have played a very important role in this direction. DFT calculations (PBE $+ U$) by Walsh *et al.* [11] reported a direct energy gap of 1.67 and 1.23 eV for Co_3O_4 at Γ and X high symmetry points of Brillouin zone, respectively. Considering $U = 4.4$ eV for Co^{2+} ions and 6.7 eV for Co^{3+} ions, Chen *et al.* [24] showed a minimum energy band gap of 1.96 eV at X point with an antiferromagnetic configuration of spins at A sites for PBE and ferromagnetic configuration for PBE $+ U$. Hereafter we use eV units for U without specifying it everywhere in the rest of the paper. Using hybrid functionals, Lima [25] reported energy band gap values between 0.35 and 2.58 eV at the X high symmetry point of the Brillouin zone. In another work, Lima [26] demonstrated that the antiferromagnetic configuration is energetically more favorable than the ferromagnetic configuration of Co_3O_4, and obtained the energy band gap 1.60 and 2.04 eV for $U = 3.0$ and 4.4, respectively. Selcuk *et al.* [27] calculated the energy band gap (E_g) of Co_3O_4 for $U = 0.0$, 3.0, and 5.9 and obtained the energy band gap 0.24, 1.13, and 1.80 eV, respectively. Using PBE $+ U$ (with $U = 2.0$), Xu *et al.* [28] computed the electronic transitions for Co_3O_4: (i) 2.2 eV due to $O(2p) \rightarrow Co^{2+}(t_{2g})$, (ii) 2.9 eV due to $O(2p) \rightarrow$

$Co^{3+}(e_g)$, and (iii) 3.3 eV due to $Co^{3+}(t_{2g}) \rightarrow Co^{2+}(t_{2g})$. Such kind of detailed theoretical study is completely lacking in the literature for the case of other magnetic inverse spinels, such as Co_2SnO_4, Co_2TiO_4, and Co_2RuO_4, which is the main focus of this article. Based on the first-principles DFT$+U$ calculations, we study the electronic and magnetic structure of Co_3O_4 for different values of U with a special emphasis on the magnetic dilution with elements such as Ti, Ru, and Sn at the octahedral sites.

The outline of this article is as follows: In Sec. II we present the computational technique and experimental methods used for the present study. Section III presents the results of our studies. Here first we compare the structural properties obtained from the experimental investigations and predicted from *ab initio* calculations. Second, we discuss the electronic structure followed by the magnetic and optical properties of both pristine and doped compounds. Finally, we conclude the salient features of this work in Sec. IV.

II. COMPUTATIONAL METHODS AND EXPERIMENTAL DETAILS

We have employed the density functional theory (DFT) based calculations to probe the electronic structure [29,30] and magnetic properties of the spinel cobaltites. We use Vienna *ab initio* simulation package (VASP) software to perform all DFT calculations [31–33]. A Monkhorst-Pack type $8 \times 8 \times 8$ k grid is used to perform integrations in the Brillouin zone. Periodic boundary conditions are employed in all directions. The Kohn-Sham equations are solved self-consistently [30] using the projector augmented wave (PAW) basis set [34,35]. A plane-wave basis set with an upper threshold value of 500 eV is employed. The exchange correlation part of the Hamiltonian is treated with the Perdew-Burke-Ernzerhof (PBE) GGA functional [36]. To begin the calculations, we take 2 formula units of the spinel primitive cell. After this the structure is optimized, first relaxing the internal positions, followed by relaxation of volume and shape using self-consistent DFT [37]. Subsequently the relaxed configuration is used to obtain the required density of states (DOS) and electronic band structure. Strong on-site Coulomb interactions are treated using DFT $+ U$ approach. We have adopted the effects of on-site Coulomb correlation and Hund's coupling within the Dudarev's approach [38]. The coupling is represented through an effective parameter $U_{\text{eff}} = U - J$, where U is the strength of the Coulomb interaction and J is the Hund's coupling constant. For all calculations, J is considered to be 0 eV. The Coulomb parameter U is considered in the range 2–6 for both octahedral and tetrahedral sites of Co. The electronic self-consistency is continued until the energy convergence is of the order of 10^{-7} eV. Structural relaxations are performed until the residual forces on each atom converge to less than 10^{-4} eV/Å.

On the other hand, the experimental details consist of both synthesis procedure and various characterization details. All the compounds are prepared by standard solid-state reaction method using stoichiometric amounts of binary transition-metal oxides GeO_2, Al_2O_3, TiO_2, RuO_2, SnO_2, and Co_3O_4 as precursors. A suitable amount of these compounds were first grinded in an agate mortar and pestle, and pressed into

cylindrical pellets of diameter 13–15 mm using a hydraulic press (40 kN). Finally, all these pellets were sintered at 1200 °C for 12 h in air except Co_2SnO_4 pellets which were first ball milled and sintered at higher temperatures 1350 °C for 12 h in air to avoid the formation of SnO_2. The phase purity and crystal structure information was investigated using the x-ray powder diffractometer from Rigaku, TTRAX III with Cu-$K\alpha$ radiation of wavelength $\lambda = 1.5406$ Å as source. Diffraction patterns of all the systems are refined with the Fullprof-Rietveld-Refinement suite [39]. Magnetic measurements at various temperatures between 2 and 330 K were performed using a superconducting quantum interference device (SQUID) based magnetometer MPMS from Quantum Design. For the optical characterization we used a spectrometer (Perkin Elmer Lambda-950) with diffusive reflectance accessory (DRA) working in the wavelength range of 200–800 nm.

III. RESULTS AND DISCUSSION

In this section we present our results on the electronic and magnetic structures of Co_3O_4, Co_2GeO_4, Co_2AlO_4, Co_2TiO_4, Co_2RuO_4, and Co_2SnO_4. In order to study the effect of strong on-site Coulomb interaction on the crystal structure, electronic, and magnetic properties, we vary U for Co ion from $U = 2$–6, while keeping U fixed for the dopants. The interactions between crystal fields and the valence electrons play an important role in deciding the magnetic, electronic, and optical behavior of these spinels. In Fig. 1 we show a schematic diagram of energy levels splitting in the presence of crystal fields. The occupations of the valence d orbital electrons of Co and Ru for both tetrahedral and octahedral sites are also shown explicitly. In Co_3O_4, Co^{2+} ion occupies the tetrahedral site, having high spin state, whereas Co^{3+} occupies the octahedral site with a low spin state. However, the inverse spinels Co_2TiO_4 and Co_2SnO_4 display different electronic configurations: Co^{2+} ions occupy both the tetrahedral and octahedral sites and the remaining half of the octahedral sites are filled by the nonmagnetic ions, whereas in case of Co_2RuO_4, the tetrahedral sites are occupied by the divalent Co and the octahedral sites are equally shared by Co^{3+} and Ru^{3+}. Interestingly, when Co_3O_4 is diluted with Ge, it retains the normal spinel structure where Ge^{4+} occupies the tetrahedral sites and both Co^{2+} ions occupy the octahedral sites.

A. Structural properties

In this section we discuss the experimental results of crystal structure data obtained from the x-ray powder diffraction. Figure 2 shows the x-ray powder diffraction pattern together with the Miller indices of different compounds. We also performed Rietveld refinement to the experimentally obtained diffraction patterns using the Fullprof-Rietveld-Refinement Suite. All the diffraction patterns except the pristine compound Co_3O_4 and Co_2GeO_4 (which belongs to normal spinel structure) correspond to the family of inverse spinel crystal structure with space group Fd–$3m$ (227). In order to probe the minute changes occurring in the crystal structure due to the dilution of different nonmagnetic elements in
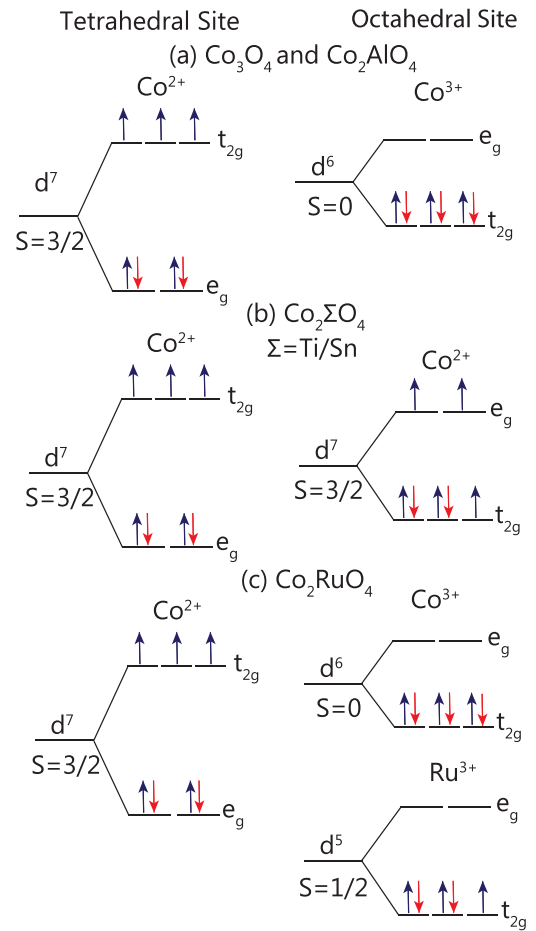

FIG. 1. A schematic diagram of the electronic band splitting on the tetrahedral (left) and octahedral (right) sites of Co and Ru 3d electron in Co_3O_4 and $Co_2\Sigma O_4$ ($\Sigma \equiv$ Al, Ti, Ru, Sn).

Co_3O_4 we have evaluated the average bond angle (Θ_{A-O-B}) and bond lengths (l_{B-O}). For Co_3O_4 the lattice parameters obtained from the x-ray diffraction experiments is of the order $a = 8.08 \pm 0.02$ Å. However, for the inverse spinels Co_2AlO_4, Co_2TiO_4, Co_2RuO_4, and Co_2SnO_4 we obtained $a = 8.09 \pm 0.03$, 8.45 ± 0.01, 8.29 ± 0.01, and 8.66 ± 0.02 Å, respectively. These diffraction patterns confirm the monophase nature of the samples prepared from the solid-state reaction method.

In Table I we list the DFT + U calculated lattice parameters and the oxygen parameters for the normal spinel Co_3O_4 and Co_2GeO_4, as well as the inverse spinels after incorporating the nonmagnetic elements at the octahedral sites. For all the compounds we observe that the lattice parameter a gradually increases with increase of U_{Co} (for the pristine compound Co_3O_4, a changes from 8.11 to 8.14 Å with increasing U_{Co} from 2 to 6). These values are in good agreement with the experimentally observed data [9–11]. For the case of Co_2SnO_4 we observed larger unit-cell volume ($V_{UC} \sim$ 679.1 Å^3 for $U_{Co} = 2$ and 683.8 Å^3 for $U_{Co} = 6$) owing to the fact that Sn^{4+} has a bigger ionic radius (0.69 Å). However, for Co_2RuO_4 (with Ru^{3+} ionic radius 0.68 Å) a large increase in V_{UC} ($\Delta V_{UC}/V_{UC} \sim 9.6\%$) was noticed as U_{Co} increases from
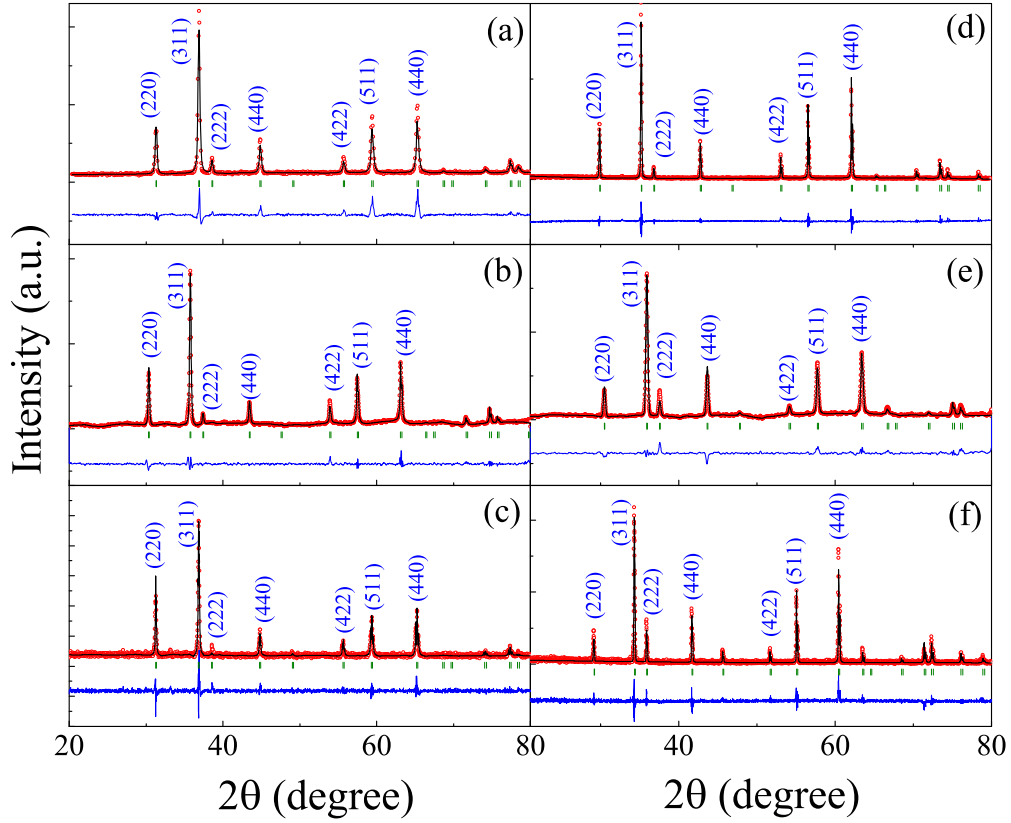
FIG. 2. XRD pattern together with the Rietveld refinement data of various Co spinels: (a) Co_3O_4, (b) Co_2GeO_4, (c) Co_2AlO_4, (d) Co_2TiO_4, (e) Co_2RuO_4, and (f) Co_2SnO_4. The red hollow symbols represent the experimental data and black solid continuous line is for the data obtained using Rietveld refinement. The blue lines at the bottom represent difference pattern observed from experiment and refinement data.

2 to 6, whereas no significant change in V_{UC} was observed for the Co_2TiO_4 [with Ti^{4+} (0.61 Å)], Co_2AlO_4 [with Al^{3+} (0.54 Å)], and Co_2GeO_4 [with Ge^{4+} (0.39 Å)]. Our results are in good agreement with the numerical work carried out by Walsh *et al.* [11]. These authors reported the lattice constants 8.11 and 8.16 Å, respectively, for normal spinel Co_3O_4 and inverse spinel Co_2AlO_4. These observations are consistent with our results ($a_{Co_3O_4}$ = 8.11 Å and $a_{Co_2AlO_4}$ = 8.13 Å).

On the other hand, we have evaluated the equilibrium bond lengths as (i) Co_{tet}-O = 1.95 Å and (ii) Co_{oct}-O = 1.93 Å for Co_3O_4, and Co_{tet}-O = 2.03 Å and Co_{oct}–O_{AVG} = 2.14 Å for inverse spinel Co_2SnO_4. Table II summarizes all the structural

parameters including the bond lengths and bond angles for different normal and inverse spinels. These values are in agreement with the previously reported numerical and experimental observations [11,15–19]. Note that the bond angle ($\Theta_{O\text{-}A\text{-}O}$) exhibits some deviation from the ideal value (109.5°) although the compound retains the global symmetry. This could be attributed to the local distortion arising from the imbalanced electronic configuration of dopant [7,40].

Figure 3 shows the variation of $\Theta_{A\text{-}O\text{-}B}$ and $l_{B\text{-}O}$ as a function of ionic radius (r) of different elements. The red colored solid spheres represent the experimental data, whereas the square symbols represent the theoretical predictions. $\Theta_{A\text{-}O\text{-}B}$

TABLE I. Calculated lattice constants (Å) and oxygen parameters [uuu] of cobalt oxides (Co_3O_4) and cobalt based spinels [$Co_2\Sigma O_4$ ($\Sigma \equiv$ Al, Ti, Ru, Sn, Ge)] for different values of U for cobalt and $U = 2$ for Ti and Ru. $U = 0$ was considered for Al, Sn, and Ge.

	Lattice parameter (Å)						Oxygen parameter		
	Coulomb interaction U (eV)					Expt.	$U = 2.0$ (eV)		
Composition	2.0	3.0	4.0	5.0	6.0		u_x	u_y	u_z
Co_3O_4	8.11	8.12	8.14	8.14	8.14	8.08	0.2634	0.2634	0.2634
Co_2GeO_4	8.42	8.42	8.42	8.43	8.43	8.33	0.2514	0.2514	0.2481
Co_2AlO_4	8.13	8.14	8.15	8.16	8.17	8.09	0.2654	0.2654	0.2602
Co_2TiO_4	8.53	8.55	8.56	8.57	8.57	8.45	0.2692	0.2692	0.2692
Co_2RuO_4	8.30	8.33	8.35	8.35	8.56	8.29	0.2558	0.2558	0.2749
Co_2SnO_4	8.79	8.80	8.80	8.81	8.81	8.66	0.2639	0.2639	0.2538

TABLE II. The equilibrium bond lengths and bond angles for Co_3O_4 and $Co_2\Sigma O_4$ (Σ = Ge, Al, Ti, Ru, Sn) obtained from DFT+U calculations using $U = 2$ eV are presented. Experimental values obtained from the x-ray diffraction measurements are given in square brackets. In the diluted $Co_2\Sigma O_4$ spinels, we noticed a Jahn-Teller type distortion at the octahedral sites. Bond lengths (l_{B-O}) and bond angles (Θ_{O-B-O}) at B site are given for each asymmetric octahedral configuration. All lengths are in Å units and angles are in degrees.

Composition	l_{A-O} (Å)	l_{B-O} (Å)	l_{A-B} (Å)	l_{B-B} (Å)	Θ_{O-A-O} (°)	Θ_{O-B-O} (°)	Θ_{A-O-B} (°)
Co_3O_4	1.95	1.93	3.36	2.87	109.5	83.3	120.7
$(Co^{2+})[Co^{3+}, Co^{3+}]O_4$	[1.94]	[1.92]			[109.5]	[83.3]	[120.6]
Co_2GeO_4	1.83	2.08, 2.11 (Co-O)	3.51 (Ge-Co)	2.98	109.2	89.5, 90.5 (Co-O-Co)	125.2 (Ge-O-Co)
$(Ge^{4+})[Co^{2+}, Co^{2+}]O_4$	[1.98]	[1.99]					[121.1]
Co_2AlO_4	1.95	1.93	3.37 (Co-Al)	2.88	109.4	84.0, 95.8 (O-Al-O)	119.9 (Co-O-Co)
			3.37 (Co-Co)	2.88		82.5, 97.5 (O-Co-O)	121.4 (Co-O-Al)
$(Co^{2+})[Al^{3+}, Co^{3+}]O_4$	[1.93]	[1.93]			[109.5]	[84.8]	[118.3]
Co_2TiO_4	1.97	1.99, 2.02 (Ti-O)	3.53 (Co-Ti)	3.01	109.8	88.5, 91.5 (O-Ti-O)	122.1 (Co-O-Ti)
		2.07, 2.16 (Co-O)	3.50 (Co-Co)		108.5	82.7, 97.3 (O-Co-O)	121.1 (Co-O-Co)
$(Co^{2+})[Ti^{4+}, Co^{2+}]O_4$	[1.98]	[2.03]					[121.7]
Co_2RuO_4	1.98	2.04, 2.06 (Ru-O)	3.46 (Co-Ru)	2.95	111.3	86.5, 93.5 (O-Co-O)	121.8 (Co-O-Co)
		1.95, 1.97 (Co-O)	3.42 (Co-Co)			82.4, 97.6 (O-Ru-O)	118.7 (Co-O-Ru)
$(Co^{2+})[Ru^{3+}, Co^{3+}]O_4$	[1.98]	[1.98]			[114.3]	[85.2]	[123.9]
Co_2SnO_4	2.03	2.10, 2.18 (Co-O)	3.62 (Co-Sn)	3.09	109.6	85.1, 94.9 (O-Co-O)	123.4 (Co-O-Co)
		2.11, 2.08 (Sn-O)	3.62 (Co-Co)			92.9, 87.1 (O-Sn-O)	121.4 (Co-O-Sn)
$(Co^{2+})[Sn^{4+}, Co^{2+}]O_4$	[1.88]	[2.16]			[114.3]	[85.2]	[125.0]

values increase progressively with increasing r. Up to $r = 0.61$ Å the experimental data of Θ_{A-O-B} agree quite well with DFT results, but for $r \geqslant 0.68$ Å a systematic deviation was observed [$(\Theta_{A-O-B})_{AVG} \sim 120.3°$ for $r_{Ru} = 0.68$ Å and $(\Theta_{A-O-B})_{AVG} \sim 122.4°$ for $r_{Sn} = 0.69$ Å]. However, this variation is within 3%, which can be ascribed to the limitations of the generalized gradient PBE approximation. The variation of average bond lengths l_{B-O} increases with increasing r ($l_{B-O} = 2.06$ Å for $r_{Ti} = 0.61$ Å and $l_{B-O} = 2.12$ Å for $r_{Sn} = 0.69$ Å). Figure 4 shows deviation in bond angle $\Delta\Theta = (\Theta_{A-O-B_{Co_2\Sigma O_4}} - \Theta_{A-O-B_{Co_3O_4}})/ \Theta_{A-O-B_{Co_3O_4}}$ and bond length $\Delta l = (l_{B-O_{Co_2\Sigma O_4}} - l_{B-O_{Co_3O_4}})/ l_{B-O_{Co_3O_4}}$ of $Co_2\Sigma O_4$ ($\Sigma \equiv$ Ge, Al, Ti, Ru, Sn) from the pristine compound Co_3O_4. For Co_2TiO_4, the experimental data are in good agreement with

the theoretical results ($\Delta\Theta \sim 1.16$). However, with the increasing size of dopants ($r \geqslant 0.68$) significant variation was noticed in the experimental ($\Delta\Theta_{A-O-B} = 2.74$ for $r_{Ru} = 0.68$ Å and $\Delta\Theta_{A-O-B} = 3.65$ for $r_{Sn} = 0.69$ Å) and theoretical ($\Delta\Theta_{A-O-B} = 0.37$ for $r_{Ru} = 0.68$ Å and $\Delta\Theta_{A-O-B} = 1.27$ for $r_{Sn} = 0.69$ Å) results. On the other hand, deviations in Δl match quite well for all the compounds except for Co_2TiO_4 where a small deviation was observed between the theoretical and experimental values. We expect that such deviations play a significant role on the magnetic exchange interactions and electronic properties of the material. In the following section we present the electronic structure obtained from our DFT + U calculations.
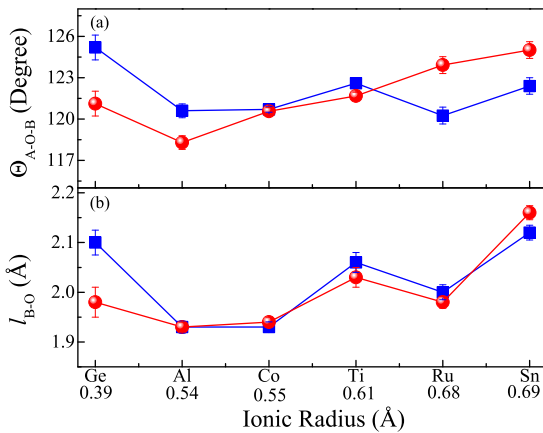

FIG. 3. Variations of (a) bond angle (Θ_{A-O-B}) and (b) bond length (l_{B-O}) with the ionic radius of the dilutants. Red solid spheres represent the experimental data, whereas the blue squares represent the theoretical predictions for $U = 2$.

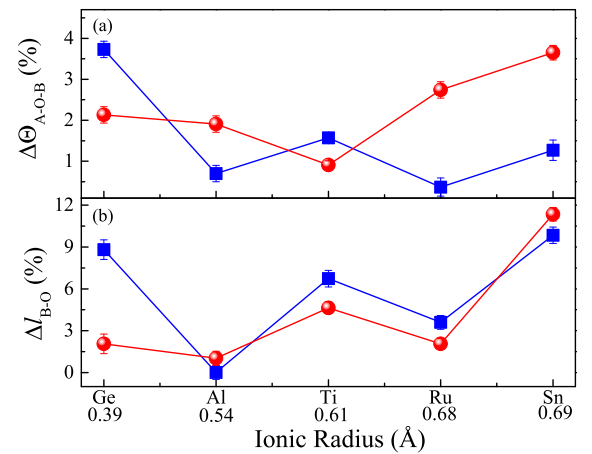FIG. 4. Deviation of (a) bond angle ($\Delta\Theta_{A-O-B}$) and (b) bond length (Δl_{B-O}) of different compound $Co_2\Sigma O_4$ (Σ = Ge, Al, Ti, Ru, Sn) compared to pristine compound Co_3O_4. Red solid spheres represent the experimental data, whereas the blue squares represent the theoretical predictions for $U = 2$.
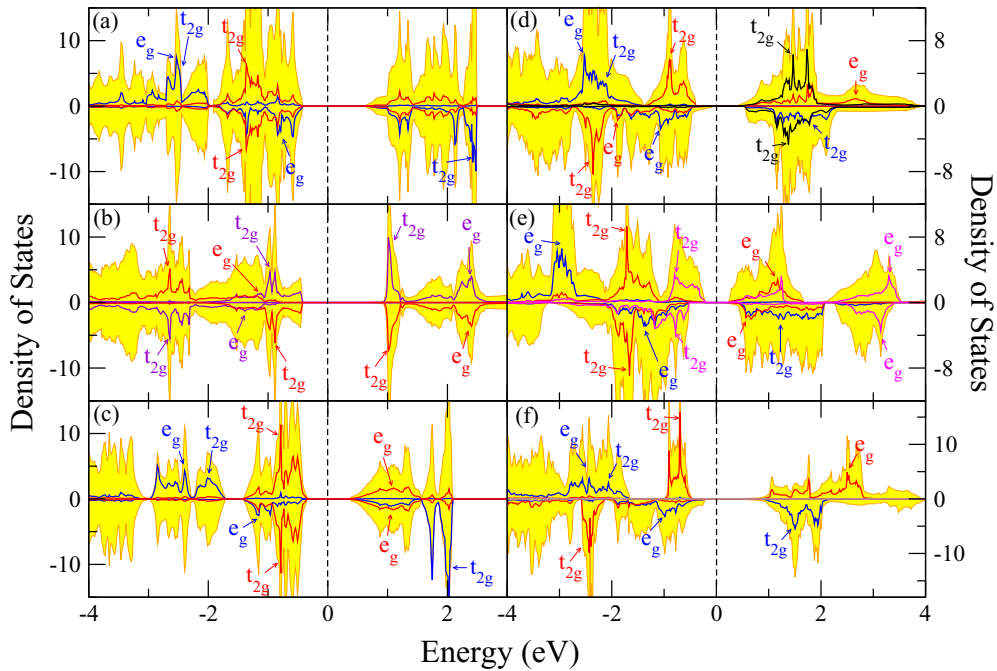
FIG. 5. Total and atom-projected electronic density of states calculated using $U = 2$: (a) Co_3O_4, (b) Co_2GeO_4, (c) Co_2AlO_4, (d) Co_2TiO_4, (e) Co_2RuO_4, and (f) Co_2SnO_4. The total density of states are represented using the yellow shade. The blue and red lines represent, respectively, the density of states related to the Co present in the tetrahedral and octahedral sites. The color codes represent: solid black lines (Ti), magenta (Ru), and brown (Sn). The solid violet line in (b) represents contribution from the other octahedral Co of Co_2GeO_4. Dotted vertical line at $E = 0$ depicts the Fermi level. The partial density of states of Sn and Ge are not visible due to their small magnitude intensity.

B. Electronic density of states

In Fig. 5 we show the density of states for Co_3O_4, Co_2GeO_4, Co_2AlO_4, Co_2TiO_4, Co_2RuO_4, and Co_2SnO_4 for the antiferro/ferrimagnetic configuration with $U = 2$ for the Co ions. For tetrahedral Co in Co_3O_4, a splitting in the minority spins of t_{2g} and e_g states is observed at $E = 2$ and -1.3 eV, respectively [Fig. 5(a)]. The $e_g^\downarrow$ (down-spin) states (minority spins) appear to be localized around the valence band ($E = -0.8$ eV), while the $t_{2g}^\downarrow$ states are situated far away from the Fermi level in the conduction band at $E \sim 2.5$ eV. The up-spin states majority spins of $t_{2g}^\uparrow$ and $e_g^\uparrow$ remain isolated and appears distinctly at the energies $E = -2.5$ eV [Fig. 5(a)]. However, for octahedrally coordinated Co, we obtain a low spin state ($S = 0$), which is quite evident from the equal contributions of the majority and minority spin states near Fermi level. For Co_2GeO_4 we find that the $e_g^\uparrow$ and $e_g^\downarrow$ states of the octahedral Co exhibit peaks around -1.39 and -2.62 eV, respectively. On one hand, $t_{2g}^\uparrow$ states are localized around top of the valence band maximum (~ -0.88 eV) and the conduction band minimum (~ 1.02 eV). Interestingly, both octahedral Co ions compensate each other contribution and exhibit stable antiferromagnetic configuration in Co_2GeO_4 [see Fig. 5(b)]. The contribution from Ge is quite negligible in the total density of states near the Fermi level. The electronic states of Co_2AlO_4 appear same as those of Co_3O_4 [see Fig. 5(c)]. The $t_{2g}^{\uparrow\downarrow}$ states of tetrahedral Co occupy at the energy of -2.4 and 2 eV, whereas the octahedrally coordinated Co are localized at the top of the valence band ($E \sim -0.4$ eV).

As we look at these details meticulously regarding the role of dilution on the density of electronic states on Co_3O_4,

several interesting observations emerge. For example, in the inverse spinel Co_2TiO_4, the energy gap appears at 0.57 eV. The $t_{2g}^\uparrow$ states are localized away from the Fermi level around energy ~ -2.1 eV, whereas the $t_{2g}^\downarrow$ states are located around 1.8 eV. For the octahedrally coordinated Co, $e_g^\uparrow$ and $e_g^\downarrow$ states are localized at the energies $E \sim 2.66$ and -1.90 eV, respectively, with negligible contribution, and for $t_{2g}^{\uparrow\downarrow}$ states, these are centered at ~ -0.9 ($t_{2g}^\uparrow$) and -2.3 eV ($t_{2g}^\downarrow$). Here our results indicate that t_{2g} states (~ 1.73 eV) of octahedrally coordinated Ti contributes quite significantly to the conduction band, while the e_g states appear to be delocalized between -2 and -6 eV. Interestingly, Ru and Sn dilution result in the localization energy at -2.9 and -2.06 eV, respectively, as compared to -2.1 eV for Co_2TiO_4. Thus, the energy gap decreases to 0.46 eV for Co_2RuO_4 as compared to the pristine compound and is minimum among all the inverse spinels. This may be the reason why Co_2RuO_4 exhibits drastic reduction in long-range magnetic ordering (~ 16 K) as compared to 47.8 K for Co_2TiO_4 and 30 K for Co_3O_4 [9,10,16–18]. As we see the detailed electronic structure we found that $t_{2g}^\uparrow$ and $e_g^\uparrow$ states of tetrahedrally coordinated Co are localized around -2.9 eV, whereas the down-spins states of $t_{2g}^\downarrow$ appear to be completely delocalized from the minimum of the conduction band [exhibiting a peak around the energy 1.3 eV as shown by the arrow mark in Fig. 5(e)]. For the octahedrally coordinated Co, the majority and minority spins of t_{2g} states are more symmetric as compared to the e_g states which lead to the low spin state. On the other hand, the t_{2g} states of the octahedrally coordinated Ru appear to localize at the vicinity of the valence band maximum (~ -0.8 eV), and the
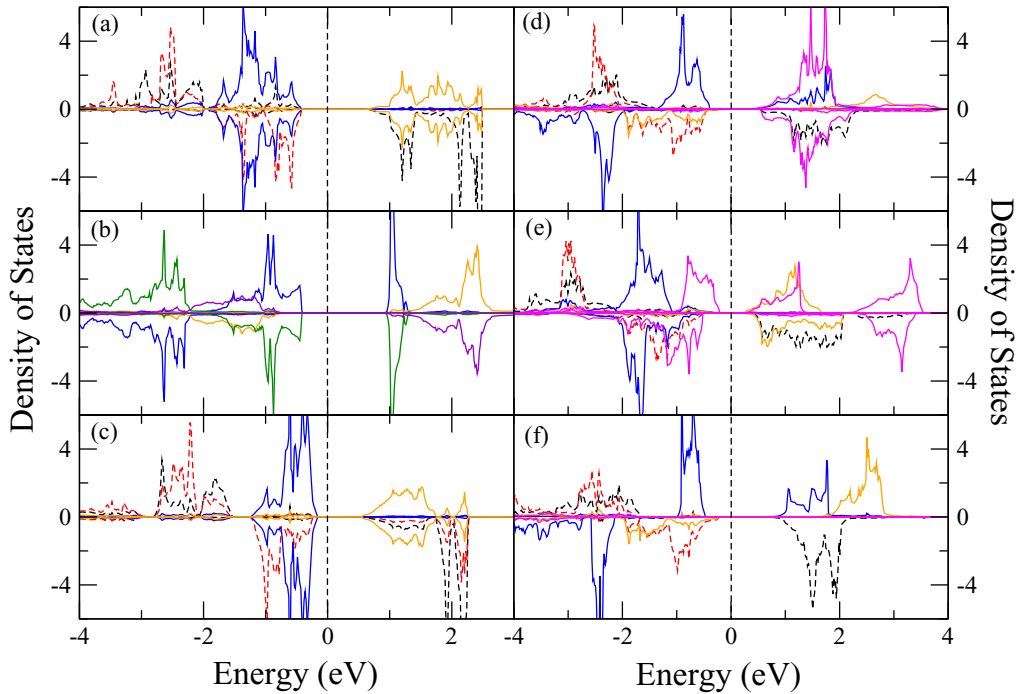
FIG. 6. Atom-projected electronic density of states calculated using $U = 2$: (a) Co$_3$O$_4$, (b) Co$_2$GeO$_4$, (c) Co$_2$AlO$_4$, (d) Co$_2$TiO$_4$, (e) Co$_2$RuO$_4$, and (f) Co$_2$SnO$_4$. For tetrahedral Co, the black and red dotted lines represent the density of t_{2g} and e_g states, respectively. For octahedral Co, the blue and orange solid lines represent the density of t_{2g} and e_g states, respectively. In case of Co$_2$GeO$_4$, the density of t_{2g} and e_g states of second octahedral Co is denoted by a solid green and violet line, respectively. The solid magenta line represents the density of states of dilutants $\Sigma \equiv$ Ge, Ti, Ru, and Sn. Dotted vertical line at $E = 0$ depicts the Fermi level. The partial density of states of Sn and Ge are not visible due to their lower intensity.

corresponding e_g states are located far away from the Fermi level (~ 3.2 eV).

Figure 5(f) shows the contribution of electronic states across the Fermi level for Co$_2$SnO$_4$ indicating the narrowing down of the overall energy gap ($\geqslant 0.7$ eV) as compared to the pristine compound Co$_3$O$_4$. As far as the electronic state contributions are concerned at the octahedral and tetrahedral sites, we found that $t_{2g}^{\downarrow}$ and $e_g^{\uparrow}$ states split around 1.7 and -2.5 eV, respectively, for Co atoms located at the tetrahedral sites. A detailed interpretation of this result provides the evidence that the $t_{2g}^{\uparrow}$ states are localized at -2.1 eV, whereas the $e_g^{\uparrow}$ and $e_g^{\downarrow}$ states are localized at -2.5 and -1.0 eV, respectively. Nevertheless, the octahedrally coordinated Co ion does not show any signatures of splitting of the bands [as shown in Fig. 5(f)]. Here the $e_g^{\uparrow}$ states are more delocalized as compared to the $e_g^{\downarrow}$ states (-1.8 eV). For octahedrally coordinated Sn, the t_{2g} states hardly contribute to the total density of states near the Fermi level. Note that partial density of states for Ge and Sn are not visible due to their lower intensity (± 0.05 states/eV for Ge and ± 0.3 states/eV for Sn) compared to the other cations.

Overall we find that the doping has important consequences on the electronic structure of the cobalt spinels. It is quite evident from our study that Co$_3$O$_4$ exhibit strong hybridization between the majority spins in $t_{2g}^{\uparrow}$ and $e_g^{\uparrow}$ states of tetrahedral cobalt (see Fig. 6) [41]. This hybridization becomes weaker for diluted compounds except for Co$_2$RuO$_4$ which exhibits identical hybridization strength as that of undoped Co$_3$O$_4$. Another important feature we noticed is

the hybridization of the minority spins at t_{2g} and e_g in the vicinity of valence band of Co$_3$O$_4$ which become quite feeble for Co$_2$RuO$_4$ and Co$_2$AlO$_4$, due to the reduction of a Co atom at the octahedral sites. It is interesting to note that this hybridization is not at all present in Co$_2$TiO$_4$ and Co$_2$SnO$_4$ as the octahedrally coordinated Co possess different electronic states (see Fig. 1). The hybridization of $t_{2g}^{\uparrow}$ and $e_g^{\uparrow}$ states at the octahedral Co site is also observed in Co$_3$O$_4$ which remain absent for the diluted systems Co$_2$AlO$_4$ and Co$_2$RuO$_4$. Nevertheless, in Co$_2$TiO$_4$ and Co$_2$SnO$_4$ we observe a weaker hybridization of down spins of Co e_g states occupying the tetrahedral and octahedral sites.

At this stage we wish to compare the effect of dilution on the exchange and crystal field splitting of all the inverse spinels. We have calculated the exchange splitting (Δ_{EX}) and crystal field splitting (Δ_{CF}) from the density of states of the materials using: (a) $\Delta_{\text{EX}}^{e_g} = e_g^{\uparrow} - e_g^{\downarrow}$, (b) $\Delta_{\text{EX}}^{t_{2g}} = t_{2g}^{\uparrow} - t_{2g}^{\downarrow}$, (c) $\Delta_{\text{CF}}^{\uparrow} = e_g^{\uparrow} - t_{2g}^{\uparrow}$, and (d) $\Delta_{\text{CF}}^{\downarrow} = e_g^{\downarrow} - t_{2g}^{\downarrow}$. Accordingly, Table III summarizes the exchange splitting (Δ_{EX}) and crystal field splitting (Δ_{CF}) parameters for the pristine and diluted spinels (for $U = 2$) in which Co^{2+} ions occupy the tetrahedral site only for all the compounds, except Co$_2$GeO$_4$ where Ge^{4+} occupies the tetrahedral sites. The magnitude of $\Delta_{\text{EX}}^{e_g}$ remains nearly constant for all the compounds and $\Delta_{\text{EX}}^{t_{2g}}$ gradually decreases upon increasing the lattice parameter varying up to 3.6 eV for Co$_2$SnO$_4$ ($a = 8.79$ Å), except Co$_2$GeO$_4$ ($r_{\text{Ge}} = 0.39$ Å). In the present case for the normal spinel Co$_3$O$_4$ the calculated values of $\Delta_{\text{EX}}^{e_g}$ and $\Delta_{\text{EX}}^{t_{2g}}$ are 1.8 and 5.2 eV, respectively. The crystal field splitting (Δ_{CF}) changes drastically

TABLE III. Exchange splitting (Δ_{EX}) and crystal field splitting (Δ_{CF}) for Co_3O_4 and $Co_2\Sigma O_4$ (Σ = Ge, Al, Ti, Ru, Sn) for $U = 2$ in eV units.

System	Ion	Tetrahedral site (in eV units)				Ion	Octahedral site (in eV units)			
		$\Delta_{EX}^{e_g}$	$\Delta_{EX}^{t_{2g}}$	$\Delta_{CF}^{\downarrow}$	$\Delta_{CF}^{\uparrow}$		$\Delta_{EX}^{e_g}$	$\Delta_{EX}^{t_{2g}}$	$\Delta_{CF}^{\downarrow}$	$\Delta_{CF}^{\uparrow}$
Co_3O_4	Co^{2+}	1.8	5.2	3.3	0.1	Co^{3+}	0.0	0.0	2.5	2.5
Co_2GeO_4	Ge^{4+}	–	–	–	–	Co_{B1}^{2+}	3.8	1.7	1.2	3.3
						Co_{B2}^{2+}	3.6	1.8	1.5	3.8
Co_2AlO_4	Co^{2+}	1.3	4.9	3.2	0.4	Co^{3+}	0.0	0.0	1.8	1.8
Co_2TiO_4	Co^{2+}	1.5	3.9	2.8	0.4	Co^{2+}	4.6	1.5	0.5	3.6
						Ti^{4+}	0.9	0.1	6.4	7.3
Co_2RuO_4	Co^{2+}	1.7	4.2	2.6	0.1	Co^{3+}	0.5	0.1	2.3	2.9
						Ru^{3+}	0.2	0.0	3.9	4.1
Co_2SnO_4	Co^{2+}	1.6	3.6	2.5	0.5	Co^{2+}	4.4	1.7	0.6	3.2

with increase in the size (r) of the diluting ions: the crystal field splitting for the down-spins ($\Delta_{CF}^{\downarrow}$) decreases from 3.3 (for $r_{Co} = 0.55$ Å) to 2.5 eV ($r_{Sn} = 0.69$ Å). The magnitude of up-spin crystal field ($\Delta_{CF}^{\uparrow}$) does not display a clear trend. For Co_3O_4 and Co_2RuO_4 the splitting values are relatively small (~0.1 eV) compared to the other compounds, Co_2TiO_4 ($\Delta_{CF}^{\downarrow} = 0.4$ eV) and Co_2SnO_4 ($\Delta_{CF}^{\downarrow} = 0.5$ eV). The Co^{3+} ions located in the octahedral crystal field do not exhibit any exchange splitting owing to its low-spin configuration. On the other hand, for octahedral Co^{3+} we observed $\Delta_{EX}^{e_g} = 0.5$ eV and $\Delta_{EX}^{t_{2g}} = 0.1$ eV in the Co_2RuO_4. This implies that the crystal field splitting does not change significantly by the substitution of Co^{3+} by Ru^{3+} at octahedral sites. For Co_2TiO_4, Co_2SnO_4, and Co_2GeO_4 the magnitudes of $\Delta_{CF}^{\uparrow}$ and $\Delta_{CF}^{\downarrow}$ are nearly identical (Table III).

C. Magnetic structure

After discussing the electronic structure based study on the observation of density of states we turn our focus on the magnetic structure of all these spinels from both theoretical and experimental results. In Table IV we have listed the magnetic moments of cations in the tetrahedral (μ_{tet}) and octahedral (μ_{oct}) sites together with the total moment (μ_{Total}) for different values of U. The unequal and opposite moments of Co at A and B sites signify the ferrimagnetic configuration all the investigated inverse spinels which is consistent with the experimental observations [6,9,10,15–20]. The magnetic moments corresponding to tetrahedral and octahedral sites increase with U. For all five studied compounds (except for Co_2GeO_4), Co^{2+} occupies tetrahedral site with a high-spin configuration ($e_g^4 t_{2g}^3$). As a result of this three unpaired electrons contribute to the total magnetic moment at the tetrahedral sites yielding magnetic moment of the order of ~3 μ_B. Our calculations yield the moment μ_{tet} between 2.53 and 2.8 μ_B for $U = 2$ and 6, respectively and these results are in good agreement with previous numerical studies by Walsh *et al.* [11].

As we discussed in the previous section the total density of states show near equal contribution from up- and down-spin states near Fermi level which implies zero net magnetic moment. The only exception is the inverse spinel with Ru dilution. This anomaly can be attributed to the presence of trivalent electronic state of Ru ions at the octahedral sites of the spinel lattice. For Ru^{3+} the magnetic moment is 0.77 μ_B

in the octahedral site, whereas the total magnetic moment is 1.92 μ_B. The corresponding magnetic moments for different values of U are listed in Table IV. Notably, recent experimental observations suggest the formation of trivalent electronic state of Ti instead of tetravalent oxidation state usually expected at the octahedral sites of inverse spinel Co_2TiO_4. Nevertheless, in our *ab initio* simulations the cubic structure is more stable for the tetravalent electronic state of Ti. The experimental observations are mainly based on the x-ray photoelectron spectroscopy measurements performed at 300 K (which is much higher than the long-range magnetic ordering considered at the DFT level) under high vacuum condition [18].

In the case of cobalt orthostannate, Co and Sn remain in divalent and tetravalent electronic configurations in the octahedral site, respectively. These results are consistent with the recent experimental studies where the divalent and tetravalent electronic configuration of Co and Sn are supported from the x-ray photoelectron spectroscopic observations [6,15,19,20]. However, the computed magnetic moment (2.6 μ_B) which is lower by $\sim37.55\%$ owing to the fact that DFT + U simulations are carried out at 0 K while the experimental studies are performed at finite temperatures above T_N [15–20]. Usually the trivalent Co exhibits a low spin configuration state for Ru diluted spinel, obtaining a magnetic moment of 0.1 μ_B. It is interesting to note that as we increase the Coulomb parameter to $U = 6$ for Co_2RuO_4 the magnetic moment of octahedral Co^{3+} increases and turns out to be 0.89 μ_B. Likewise, cobalt orthogermanate Co_2GeO_4 both the divalent Co in the octahedral sites exhibits an opposite magnetic moment of 2.60 μ_B, whereas Ge attains a nonmagnetic tetravalent configuration.

We performed the magnetization measurements at different temperatures in order to probe the effect of dilution on the magnetic ordering temperature of Co_3O_4. In what follows, we present a systematic analysis of these experimental observations. Figures 7(a)–7(f) shows the temperature dependence of magnetization $M(T)$ recorded under both zero-field-cooled (ZFC) and field-cooled (FC) conditions. The data has been recorded while heating with an external dc-magnetic field H_{dc} of 500 Oe. In the case of undoped Co_3O_4, both the magnetization curves $M_{ZFC}(T)$ and $M_{FC}(T)$ exhibits peak at 38 K [Fig. 7(a)] indicating the antiferromagnetic ordering below this temperature and paramagnetic behavior above. It is well known that the magnetic moment in Co_3O_4 arises due to the divalent Co ions ($e_g^4 t_{2g}^3$), and negligible contribution from

TABLE IV. The magnetic moment of tetrahedral (μ_{tet}) and octahedral (μ_{oct}) cations and the total moment (μ_{Total}). All the magnetic moments are calculated in Bohr magneton unit. Experimental values obtained from the previously reported neutron diffraction studies are given in square brackets.

U	System	Tetrahedral site	μ_{tet}	Octahedral site	μ_{oct}	μ_{Total}
	Co_3O_4	Co^{2+}	2.53	Co^{3+}	0.0	0.0
	Co_2GeO_4	Ge^{4+}	0.0	$Co_{B1}^{2+}/Co_{B2}^{2+}$	−2.64/2.64	0.0
	Co_2AlO_4	Co^{2+}	2.60	Co^{3+}	0.0	0.0
2.0	Co_2TiO_4	Co^{2+}	2.58	Co^{2+}/Ti^{4+}	−2.61/0.05	−0.035
	Co_2RuO_4	Co^{2+}	2.54	Co^{3+}/Ru^{3+}	0.10/−0.84	1.91
	Co_2SnO_4	Co^{2+}	2.61	Co^{2+}/Sn^{4+}	−2.62/0.03	−0.032
	Co_3O_4	Co^{2+}	2.61	Co^{3+}	0.0	0.0
	Co_2GeO_4	Ge^{4+}	0.0	$Co_{B1}^{2+}/Co_{B2}^{2+}$	−2.69/2.69	0.0
	Co_2AlO_4	Co^{2+}	2.66	Co^{3+}	0.0	0.0
3.0	Co_2TiO_4	Co^{2+}	2.65	Co^{2+}/Ti^{4+}	−2.66/0.05	−0.032
	Co_2RuO_4	Co^{2+}	2.61	Co^{3+}/Ru^{3+}	0.12/−0.87	1.92
	Co_2SnO_4	Co^{2+}	2.67	Co^{2+}/Sn^{4+}	−2.68/0.02	−0.032
	Co_3O_4	Co^{2+}	2.68	Co^{3+}	0.0	0.0
	Co_2GeO_4	Ge^{4+}	0.0	$Co_{B1}^{2+}/Co_{B2}^{2+}$	−2.74/2.74	0.0
	Co_2AlO_4	Co^{2+}	2.71	Co^{3+}	0.0	0.0
4.0	Co_2TiO_4	Co^{2+}	2.70	Co^{2+}/Ti^{4+}	2.71/0.04	−0.030
	Co_2RuO_4	Co^{2+}	2.67	Co^{3+}/Ru^{3+}	0.14/−0.89	1.94
	Co_2SnO_4	Co^{2+}	2.72	Co^{2+}/Sn^{4+}	−2.73/0.017	−0.028
	Co_3O_4	Co^{2+}	2.73	Co^{3+}	0.0	0.0
	Co_2GeO_4	Ge^{4+}	0.0	$Co_{B1}^{2+}/Co_{B2}^{2+}$	−2.78/2.78	0.0
	Co_2AlO_4	Co^{2+}	2.75	Co^{3+}	0.0	0.0
5.0	Co_2TiO_4	Co^{2+}	2.75	Co^{2+}/Ti^{4+}	−2.75/0.04	−0.028
	Co_2RuO_4	Co^{2+}	2.72	Co^{3+}/Ru^{3+}	0.2/−0.92	1.95
	Co_2SnO_4	Co^{2+}	2.76	Co^{2+}/Sn^{4+}	−2.77/0.015	−0.027
	Co_3O_4	Co^{2+}	2.78	Co^{3+}	0.0	0.0
	Co_2GeO_4	Ge^{4+}	0.0	$Co_{B1}^{2+}/Co_{B2}^{2+}$	−2.81/2.81[3.02][a]	0.0
	Co_2AlO_4	Co^{2+}	2.78	Co^{3+}	0.0	0.0
6.0	Co_2TiO_4	Co^{2+}	2.76 [2.11][b]	Co^{2+}/Ti^{4+}	−2.80/0.03 [2.89/0.72][b]	−0.027
	Co_2RuO_4	Co^{2+}	2.76	Co^{3+}/Ru^{3+}	0.89/ − 1.53[−/1.73][c]	1.99
	Co_2SnO_4	Co^{2+}	2.80 [2.04][b]	Co^{2+}/Sn^{4+}	−2.80/0.018[2.57/−][b]	-0.028

[a] Reference [45].
[b] Reference [20].
[c] Reference [16].

the spin-orbit coupling [9,10,42]. Whereas trivalent Co ions do not possess any permanent magnetic moment owing to the splitting of $3d$ levels by the octahedral crystal field and complete filling of t_{2g} levels. For this case the antiferromagnetic Néel temperature T_N (= 30 K) is estimated from the differential susceptibility curve $\partial(\chi T)/\partial T$ ($\chi = M_{ZFC}/H$) which is in good agreement with the previous experimental observations [9,43]. Almost similar features have been observed in the case of Ge diluted system (Co_2GeO_4) except the $T_N = 20.4$ K [Fig. 7(b)] which is in good agreement with the results of Hubsch and Gavoille who reported $T_N = 20.25$ K [14]. On the other hand, dilution of Co_3O_4 with Al shifts T_N significantly towards the lower temperatures ∼4.8 K. It is interesting to notice that Co_2TiO_4 exhibits completely different behavior with giant bifurcation between M_{ZFC} and M_{FC} below the ferrimagnetic ordering temperature 47.8 K, as shown by the arrow in Fig. 7(d). Such ferrimagnetic ordering is arising due to unequal magnetic moments of divalent Co ions at the tetrahedral A sites and octahedral B sites. Below this ferrimagnetic T_N magnetization curves display compensation behavior ($T_{COMP} \sim 31.6$ K) where the two sublattices balance

with each other. However, such compensation effect is very feeble which occurs at very low temperatures (∼4 K) in case of Co_2SnO_4 [Fig. 7(f)]. This system also shows ferrimagnetic ordering at 41 K which is inline with the recent experimental reports [15,19]. However, a completely distinct magnetic behavior was noticed in the case of Co_2RuO_4 where the long range ordering was collapsed which is evident below 16 K consistent with the previous reports [16].

We next focus on the pairwise magnetic exchange interactions. We compute the magnetic exchange parameters by mapping DFT + U total energies onto a Heisenberg Hamiltonian [24]: The contribution of the magnetic moment in Co_3O_4 is due to high spin state of tetrahedral Co^{2+}. We calculated the exchange coupling parameter (J_{ij}) using the Heisenberg spin Hamiltonian [24]:

$$H = -\sum_{\langle ij \rangle} J_{ij} S_i S_j, \qquad (1)$$

where i and j denote the nearest neighbor sites. The results are given in Table V. The calculated parameters are in agreement
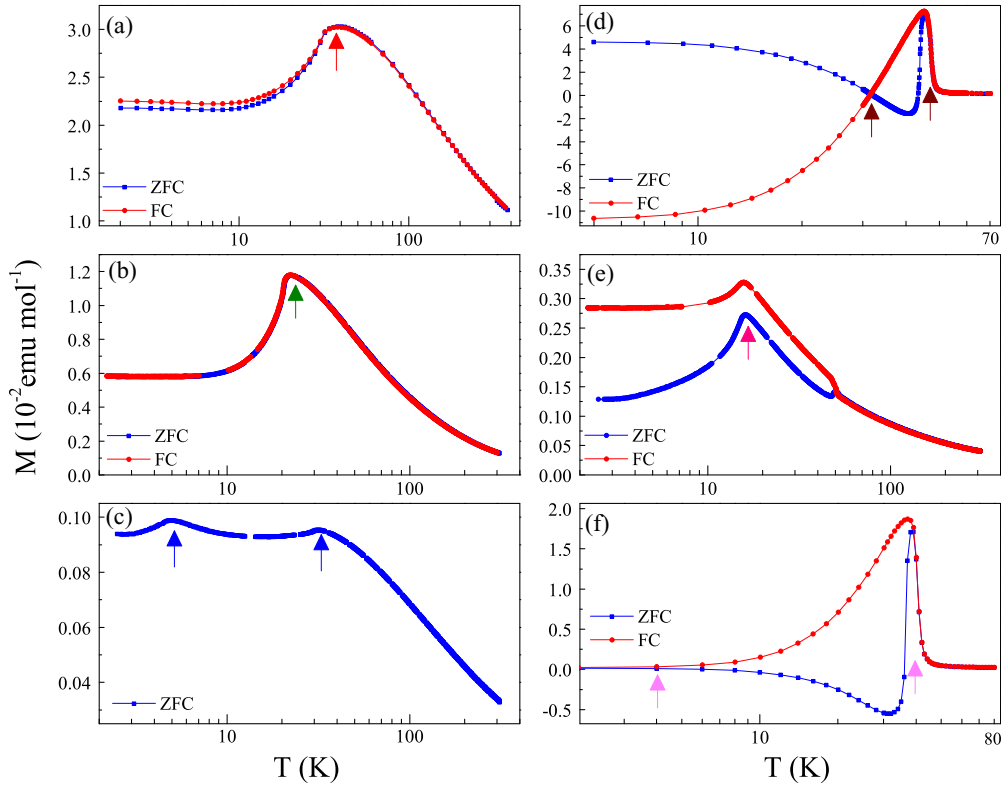
FIG. 7. The temperature dependence of magnetization measured zero-field-cooled (ZFC) and field-cooled (FC) ($H_{dc} = 500$ Oe) conditions for (a) Co_3O_4, (b) Co_2GeO_4, (c) Co_2AlO_4, (d) Co_2TiO_4, (e) Co_2RuO_4, and (f) Co_2SnO_4.

with existing results [24,44]. We find that the three exchange parameters (J_{A-A}, J_{B-B}, J_{A-B}) are all antiferromagnetic with only one exception of Co_2SnO_4. With the dilution of Ti ($r = 0.61$ Å) we observe a decrease in the strength (~ -0.84 meV) of A-A interactions. Interestingly, we observe a huge increase in the coupling strength as one goes from Co_3O_4 to Co_2RuO_4 ($J_{A-A} = -14.21$ meV). However, diluting with tetravalent Sn in the pristine compound results in dominant ferromagnetic A-A interactions with a strength of 6.4 meV. Nevertheless, at octahedral sites an antiferromagnetic configuration is stable for $Co_2\Sigma O_4$ ($\Sigma \equiv$ Ti, Ru, Sn).

TABLE V. Calculated magnetic exchange parameters (J_{ij} in meV) of Co_3O_4 and $Co_2\Sigma O_4$ ($\Sigma \equiv$ Ge, Al, Ti, Ru, Sn) for $U = 2.0$ eV. In the parentheses corresponding experimental values are mentioned.

System	J_{A-A}	J_{B-B}	J_{A-B}
Co_3O_4	$-1.73(0.65)$[a]	$0.0(0.0)$[a]	$0.0(0.0)$[a]
Co_2GeO_4	0.0	-22.31 (Co_{B1}–Co_{B2})	0.0
		-51.49 (Co_{B1}–Co_{B1})	
Co_2AlO_4	-1.33	0.0	0.0
Co_2TiO_4	$-0.84(-0.53)$[b]	$-2.57(-0.39)$[b]	$-1.50(-0.44)$[b]
Co_2RuO_4	-14.21	-7.11	-2.66
Co_2SnO_4	$6.40(0.34)$[c]	$-2.13(0.45)$[c]	$0.17(0.36)$[c]

[a] Reference [44].

[b] Reference [23].

[c] Reference [18].

The coupling strength J_{B-B} for Co_2SnO_4 and Co_2TiO_4 is -2.13 and -2.57 meV, respectively. In case of Co_2RuO_4, the coupling strength increases to -7.11 meV due to the trivalent Ru ions of magnetic moment ~ 0.9 μ_B. Such increase of magnetic moment can be attributed to the availability of unfilled spins in t_{2g} states. The exchange coupling J_{A-B} increases with increasing the size of dilutants (e.g., $J_{A-B} = -1.50$ meV for Co_2TiO_4 and $J_{A-B} = -2.66$ meV for Co_2RuO_4). For Co_2SnO_4, J_{A-B} displays the weakest coupling strength of 0.17 meV with ferrimagnetic A-B coupling. Among all the dilutants, Co_2RuO_4 possesses strong antiferromagnetic couplings between A-A (-14.21 meV), B-B (-7.11 meV), and A-B (-2.66 meV) sites. Such large interactions between the spins occur due to the larger crystal field splitting of Ru^{3+} than Co^{2+} (see Table III) further resulting in very high anisotropy which is quite evident from the experimental data (Fig. 7). Moreover, from the electronic configuration we noticed that trivalent Ru exhibits half-filled d states on B sites (d^5), whereas divalent Co exhibits unfilled d states on A site (d^7). As a result of this, the A-B coupling strength becomes prominent in Co_2RuO_4. The exchange interaction J_{A-B} also exhibits an increasing trend for Co_2TiO_4 to Co_2RuO_4. This feature can be understood from the point of view of the reduction of the bond length between the A and B cations from 3.50 to 3.42 Å for Co_2TiO_4 and Co_2RuO_4, respectively. As we compare our calculated results with the neutron diffraction results reported earlier, we find a good consistency. For example, the neutron diffraction studies carried out at $T = 1.5$ K for Ti and Sn diluted systems exhibits magnetic moment per Co^{2+} ion at the octahedral site as 2.89 and 2.57 μ_B,
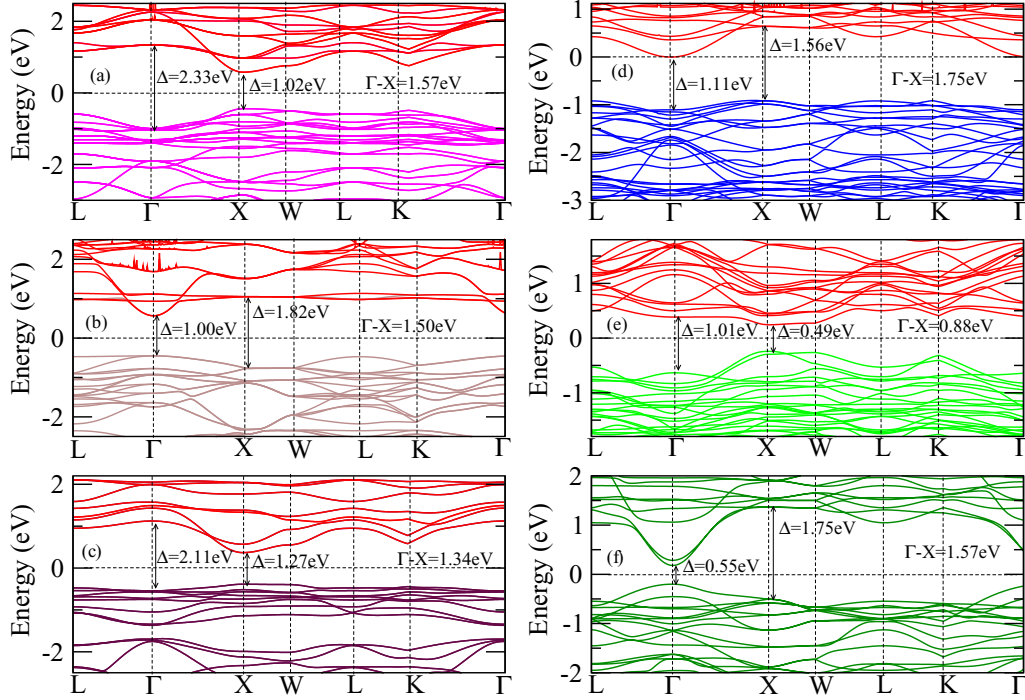
FIG. 8. Band structure is calculated using $U = 2$: (a) Co_3O_4, (b) Co_2GeO_4, (c) Co_2AlO_4, (d) Co_2TiO_4, (e) Co_2RuO_4, and (f) Co_2SnO_4 and plotted with the symmetry points in the reciprocal lattice.

respectively which are inline with the numerical results shown in Table IV [20]. Whereas the Ge system exhibits $\mu_{Co\text{-}oct} \sim 3.02 \, \mu_B$ (1.6 K) close to the calculated value 2.81 μ_B [45]. On the other hand, the Ru diluted system exhibits magnetic moment $\sim 1.73 \, \mu_B$ at 4 K for Ru^{3+}, which is close to the calculated values ($\sim 1.53 \, \mu_B$) [16]. The exchange interaction between the cations located at tetrahedral sites $J_{A\text{-}A}$ exhibits strong coupling that corroborate the current numerical results (Table V) [16].

D. Electronic band gap

In this section we focus our studies on the energy band structure of all the spinels which will be interpreted based on our experimental data related to the optical absorption performed using the diffusive reflectance spectroscopy. First we discuss our computational results obtained with different U. Figure 8 shows the electronic band structure calculated along different high symmetry directions in the reciprocal space with $U = 2$ for Co ions in different spinels. In Co_3O_4 the octahedral Co $3d$ states are mainly contributing to the conduction band, whereas the valence band maxima are formed by both tetrahedral Co $3d$ and O $2p$ states. Here we restrict our discussion to the energy band gap displayed at high symmetry points Γ and X. The direct $\Gamma-\Gamma$ and $X-X$, and the indirect $\Gamma-X$ energy band gaps are listed in the Table VI for studied compounds at different values of U.

In case of the normal spinel Co_3O_4 (for $U = 2$) the energy gap at $\Gamma-\Gamma$ and $X-X$ turns out to be 2.33 and 1.02 eV, respectively, whereas the indirect band gap at $\Gamma-X$ is 1.57 eV. These values increase with increasing U. For instance, the gap at $\Gamma-\Gamma$ increases to 3.76 and 2.70 eV at $X-X$ for $U = 6$. These band gaps calculated for the symmetry point

$X-X$ at $U = 2$ and 3, agree quite well with the previously reported results ($E_g = 1.5–2.5$ eV) [24–28,46]. It should be noted that for U values between 4 and 6 the gap appears with a higher magnitude than those previously reported theoretical values [11,24–28]. For $U = 2$ the direct $\Gamma-\Gamma$ band gap exhibits decreasing trend (e.g., $\Gamma-\Gamma_{Co_2TiO_4} = 1.11$ eV, $\Gamma-\Gamma_{Co_2RuO_4} = 1.02$ eV, and $\Gamma-\Gamma_{Co_2SnO_4} = 0.55$ eV) with the increasing size of the dilutant cations. On the other hand, the

TABLE VI. The calculated direct $\Gamma-\Gamma$ and $X-X$, and indirect $\Gamma-X$ transitions of different Co based spinel for different value of U.

U (eV)		2.0	3.0	4.0	5.0	6.0
	$\Gamma-\Gamma$	2.33	2.92	3.39	3.62	3.76
Co_3O_4	$X-X$	1.02	1.46	1.89	2.33	2.70
	$\Gamma-X$	1.57	2.09	2.52	2.73	2.85
	$\Gamma-\Gamma$	1.00	1.39	1.74	1.95	2.09
Co_2GeO_4	$X-X$	1.82	2.60	3.28	3.74	4.13
	$\Gamma-X$	1.50	2.28	2.98	3.53	3.91
	$\Gamma-\Gamma$	2.11	2.59	3.03	3.23	3.41
Co_2AlO_4	$X-X$	1.27	1.75	2.21	2.53	2.83
	$\Gamma-X$	1.34	1.81	2.23	2.44	2.64
	$\Gamma-\Gamma$	1.11	1.45	1.71	1.92	2.06
Co_2TiO_4	$X-X$	1.56	1.94	2.25	2.50	2.68
	$\Gamma-X$	1.34	2.11	2.42	2.68	2.85
	$\Gamma-\Gamma$	1.01	1.07	1.11	1.15	0.89
Co_2RuO_4	$X-X$	0.49	0.50	0.49	0.44	0.97
	$\Gamma-X$	0.88	0.92	0.95	0.94	1.30
	$\Gamma-\Gamma$	0.55	0.59	0.79	1.05	1.17
Co_2SnO_4	$X-X$	1.75	2.36	2.91	3.41	3.86
	$\Gamma-X$	1.57	2.00	2.48	3.07	3.46

TABLE VII. The calculated direct Γ–Γ and X–X, and indirect Γ–X transitions of Co_2RuO_4 for different value of U.

U (eV)		2.0	3.0	4.0	5.0	6.0
	Γ–Γ	1.01	1.07	1.11	1.15	0.89
U fixed for Ru	X–X	0.49	0.50	0.49	0.44	0.97
	Γ–X	0.88	0.92	0.95	0.94	1.30
	Γ–Γ	1.01	1.48	1.68	1.65	1.74
U fixed for Co	X–X	0.49	0.82	1.08	1.23	1.43
	Γ–X	0.88	1.34	1.58	1.60	1.66

band gap at symmetry points X–X display an increasing trend with the increasing ionic size of the dilutants. For example, $E_g(X - X) = 1.56$ and 1.75 eV for Co_2TiO_4 and Co_2SnO_4, respectively. However, for Co_2GeO_4 we find that a direct Γ–Γ and X–X band gap of 1.0 and 1.82 eV, respectively, for $U = 2$, despite Ge have the lowest ionic radius among the dopants (i.e., $r \sim 0.39$ Å). The observed band gaps for Co_2GeO_4 appear to be closer to Co_2SnO_4 which may be due to identical valence electronic structures of d orbitals in Ge^{4+} ($3d^{10}$) and Sn^{4+} ($4d^{10}$). Interestingly, with the incorporation of Ru ($r \sim 0.68$ Å) the gap at symmetry points (X–X) happens to be lowest as compared to the remaining inverse spinels (0.49 eV). For Co_2RuO_4 the band gap at Γ–Γ symmetry points remains nearly equal upon increasing U (Γ–$\Gamma = 1.02$ and 1.15 eV for $U = 2.0$ and 6.0, respectively) except for $U \geqslant 6.0$ an anomalous trend was noticed (Tables VI and VII). In order to probe the role of the d-orbital electrons and their correlations in Ru diluted compound with the band gap at the symmetry points Γ–Γ, X–X and Γ–X transitions we varied the magnitude of U for Ru from 2 to 6 while keeping fixed value of U of Co at 2. These computed data are listed in Table VII. Accordingly, we noticed a systematic increasing trend of Γ–Γ and X–X band gaps (Γ–$\Gamma_{U=3.0} = 1.48$ eV and Γ–$\Gamma_{U=6.0} = 1.74$ eV; X–$X_{U=3.0} = 0.82$ eV and X–$X_{U=6.0} = 1.43$ eV) with increasing magnitude of U of Ru. This interesting observation reveals that the vital role of strong electronic correlations in d orbital of Ru in determining the overall band-gap characteristics. Unlike other compounds where we varied only the U values of Co ions while keeping fixed values of U for dilutants Ge, Al, Ti, and Sn. The U values in Co_2RuO_4 need to be varied for both Co as well as Ru.

We performed the room temperature optical absorbance measurements using the diffuse reflectance spectroscopy (DRS) in UV visible and near IR range. For precise determination of optical band gap E_g we used the experimentally obtained reflectance data and employed the Kubelka-Munk (KM) analysis [47]. It is well known that for a parabolic shaped band structure, the KM equation can be expressed in terms of energy of a single photon $\hbar\omega$, the band gap of the system E_g (eV), and remission function or KM function as

$$[F(R_\infty)\hbar\omega]^2 = \alpha(\hbar\omega - E_g). \qquad (2)$$

In the above equation α is a constant (absorption coefficient). Figure 9(a) shows the variation of $F(R_\infty)$ as a function of photon energy ($\hbar\omega$) (eV) for the undiluted Co_3O_4 normal spinel. The inset of Fig. 9(a) represents its corresponding
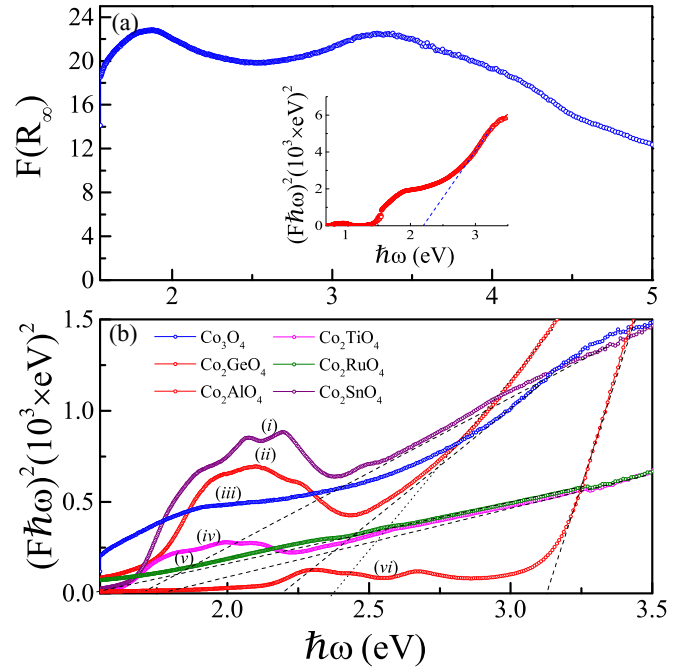

FIG. 9. (a) Experimental $F(R_\infty)$ vs photon energy $\hbar\omega$ for Co_3O_4. The inset shows the plot of $[F(R_\infty)\hbar\omega]^2$ against the photon energy $\hbar\omega$. (b) $[F(R_\infty)\hbar\omega]^2$ is plotted as a function of $\hbar\omega$ for Co_3O_4 and $Co_2\Sigma O_4$ ($\Sigma \equiv$ Ge, Al, Ti, Ru, Sn). The solid lines are the extrapolation of the linear region to determine the optical band gap E_g.

modulation function $[F(R_\infty)\hbar\omega]^2$ plotted as a function of $\hbar\omega$. Extrapolation of the band tail (as shown by the dotted lines) intercepts the x axis at $\hbar\omega = 2.19$ eV which corresponds to the direct band gap of the system which is consistent with the previously reported values for the bulk Co_3O_4 system [6,46]. Similar analysis has been performed to determine the E_g of diluted systems [Fig. 9(b)]. The left-hand side scale of Fig. 10 shows the corresponding E_g values obtained for different diluting elements and is plotted as a function of their ionic radius [0.39 Å (Ge) $\leqslant r \leqslant$ 0.69 Å (Sn)]. We compared the experimentally obtained band gap $E_{g\text{-Expt}}$ with E_g values obtained from the DFT calculations ($E_{g\text{-Theor}}$) which was plotted on the right-hand side scale of Fig. 10. Both the experimental and calculated results are consistent with each other. An overall decreasing trend has been observed in the E_g values with increasing the size of diluting element. For pristine compound Co_3O_4, experimentally obtained band gap is 2.19 eV which is quite near to the calculated value 2.33 eV. The theoretical and experimentally obtained band gaps for Co_2GeO_4 are respectively 3.28 and 3.16 eV, whereas for Co_2AlO_4 those are 2.37 and 2.59 eV, respectively (indicating high E_g compared to the normal spinel Co_3O_4). However, for Co_2TiO_4, Co_2RuO_4, and Co_2SnO_4, the band gap varies between 1.77 (for Co_2TiO_4) and 1.52 eV (for Co_2RuO_4). Table VI summarizes the $E_{g\text{-Theor}}$ values obtained from DFT + U calculations for different dilutants and different U values. Moreover, we noticed the signatures of internal d-d transitions $[t_{2g}(Co^{3+}) \rightarrow t_{2g}(Co^{2+})]$ from the experimental
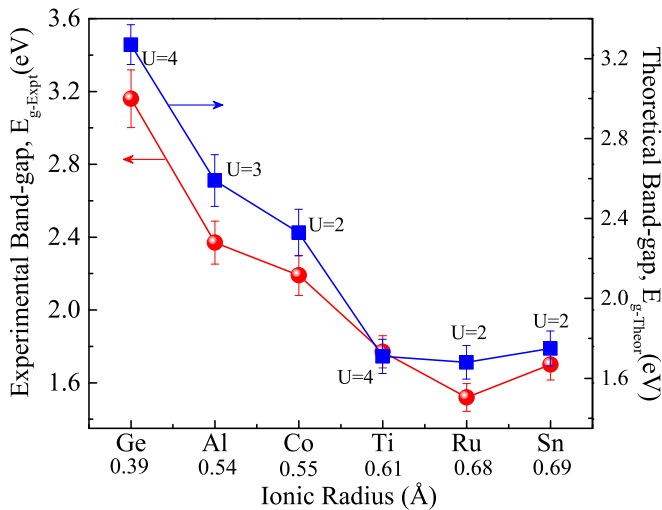
FIG. 10. The band gaps (E_g) as a function of ionic radius of the dilutants. The right panel shows the experimental band gap ($E_{g\text{-Expt}}$) and the left panel indicates the theoretical band gap ($E_{g\text{-Theor}}$) values of U_{Co} (as indicated in the figure) are chosen to obtain the theoretical result closure to the experimental observation.

$F(R_\infty)$ versus $\hbar\omega$ plots. These transitions are much prominent for the Co_3O_4 case than the diluted spinels.

IV. CONCLUSIONS

The role of magnetic dilution on the electronic structure and antiferromagnetic ordering of Co_3O_4 ($T_N = 30$ K) was successfully investigated using DFT $+ U$ calculations and experiments. We have considered the diluted form as $Co_2\Sigma O_4$ where Σ represents nonmagnetic element Ge, Al, Ti, Ru, and Sn. We find that the dilution leads to a stable inverse spinel crystal structure for all these compounds (except Co_2GeO_4, which exhibits normal spinel configuration) unlike the pristine compound Co_3O_4 in which the size of unit cell increases on replacing the octahedrally coordinated Co^{3+} ions with Σ. The numerically computed crystal structure parameters, which include bond angle, bond length, lattice constants, etc. are in good agreement with those obtained in the experiment using the Rietveld analysis of x-ray diffraction.

Our DFT calculations suggest that in Co_3O_4 the crystal field splitting ($\Delta_{CF}^{\downarrow}$) of tetrahedral divalent Co ion changes significantly (3.3–2.5 eV) with increasing the unit-cell volume (527.51–649.46 $\overset{\circ}{A}^3$) except for Co_2GeO_4, whereas the exchange splitting $\Delta_{EX}^{e_g}$ does not exhibit any significant change with increasing the size of the dopant for $U = 2$. On the

contrary, $\Delta_{EX}^{t_{2g}}$ shows a decreasing trend (5.2–3.6 eV) with increase of the lattice parameter (8.08–8.66 Å). Numerical calculations reveal an antiferromagnetic configuration for Co_2AlO_4, Co_2GeO_4, and Co_3O_4, in contrast to other inverse spinels (Co_2TiO_4, Co_2RuO_4, and Co_2SnO_4) which we found to have the tendency to form ferrimagnetic structure. These results are consistent with our magnetization measurements which yield the order parameters for antiferromagnetic Co_2AlO_4, Co_2GeO_4, and Co_3O_4 with Néel temperatures $T_N = 4.8$, 20.4, and 30 K, respectively. Whereas for the inverse spinels, ferrimagnetic Néel temperature $T_{FE-N} = 16$, 47.8, and 41 K for Co_2RuO_4, Co_2TiO_4, and Co_2SnO_4, respectively. For all these compounds, at absolute temperature, the computed intrinsic total magnetic moments are nearly zero, except Co_2RuO_4 which exhibits nonzero magnetic moment (1.91 μ_B) suggesting the restoring of magnetic moment while substituting the Co^{3+} with Ru^{3+}. This observation is consistent with the experimentally obtained temperature dependence of magnetization data where we noticed a significant shift of the magnetic-ordering temperature towards the lower value (16 K) as Co is substituted with Ru.

The Kulbelka-Munk analysis of the optical absorption spectra obtained from diffusive reflectance spectroscopy reveal that the optical band gap energy (E_g) of the spinels are in good agreement with the theoretically calculated E_g [for Co_3O_4, 2.33 eV ($E_{g\text{-Theor-}U} = 2$) and 2.19 eV ($E_{g\text{-Expt}}$)]. It was found that the E_g decreases (1.52 eV) on increasing the ionic radius ($r_{Ru} = 0.68$ Å) of the dilutant. For Co_2GeO_4 and Co_2SnO_4 the experimental band gaps (3.16 and 1.70 eV) are consistent with $X–X$ direct band gap, whereas for the remaining compound they agree well with the $\Gamma–\Gamma$ direct band gap obtained theoretically.

[1] T. Nakamura, M. Misono, and Y. Yoneda, J. Catal. **83**, 151 (1983).

[2] L. Peter and K. Wijayantha, Electrochem. Commun. **1**, 576 (1999).

[3] E. Iglesia, S. L. Soled, R. A. Fiato, and G. H. Via, J. Catal. **143**, 345 (1993).

[4] J. Xu, P. Gao, and T. Zhao, Energy Environ. Sc. **5**, 5333 (2012).

[5] Z. Wu, W. Ren, L. Wen, L. Gao, J. Zhao, C. Zhao, Z. Chen, G. Zhou, F. Li, and H. M. Cheng, ACS nano **4**, 3187 (2010).

[6] S. Thota and S. Singh, *Magnetic Spinels-Synthesis, Properties and Applications*, edited by M. S. Seehra (InTech, 2017).

[7] P. Pramanik, S. Thota, S. Singh, D. C. Joshi, B. Weise, A. Waske, and M. S. Seehra, J. Phys.: Condens. Matter **29**, 425803 (2017).

[8] S. Jin, G. Yang, H. Song, H. Cui, and C. Wang, ACS Appl. Mater. Interfaces **7**, 24932 (2015).

[9] P. Dutta, M. S. Seehra, S. Thota, and J. Kumar, J. Phys.: Condens. Matter **20**, 015218 (2007).

[10] S. Thota, A. Kumar, and J. Kumar, Mater. Sci. Eng. B **164**, 30 (2009).

[11] A. Walsh, S.-H. Wei, Y. Yan, M. M. Al-Jassim, J. A. Turner, M. Woodhouse, and B. A. Parkinson, Phys. Rev. B **76**, 165119 (2007).

[12] T. Gibb, R. Greatrex, N. Greenwood, D. Puxley, and K. Snowdon, Chem. Phys. Lett. **20**, 130 (1973).

[13] J. Hubsch and G. Gavoille, Phys. Rev. B **26**, 3815 (1982).

[14] J. Hubsch and G. Gavoille, J. Magn. Magn. Mater. **66**, 17 (1987).

[15] S. Thota and M. Seehra, J. Appl. Phys. **113**, 203905 (2013).

[16] D. Mandrus, V. Keppens, and B. Chakoumakos, Mater. Res. Bull. **34**, 1013 (1999).

[17] S. Nayak, K. Dasari, D. C. Joshi, P. Pramanik, R. Palai, A. Waske, R. Chauhan, N. Tiwari, T. Sarkar, and S. Thota, J. Appl. Phys. **120**, 163905 (2016).

[18] S. Nayak, S. Thota, D. Joshi, M. Krautz, A. Waske, A. Behler, J. Eckert, T. Sarkar, M. S. Andersson, R. Mathieu *et al.*, Phys. Rev. B **92**, 214434 (2015).

[19] S. Thota, V. Narang, S. Nayak, S. Sambasivam, B. Choi, T. Sarkar, M. S. Andersson, R. Mathieu, and M. Seehra, J. Phys.: Condens. Matter **27**, 166001 (2015).

[20] S. Thota, M. Reehuis, A. Maljuk, A. Hoser, J.-U. Hoffmann, B. Weise, A. Waske, M. Krautz, D. Joshi, S. Nayak *et al.*, Phys. Rev. B **96**, 144104 (2017).

[21] B. Antic, G. Goya, H. Rechenberg, V. Kusigerski, N. Jovic, and M. Mitric, J. Phys.: Condens. Matter **16**, 651 (2004).

[22] K. De Strooper, A. Van Alboom, C. Henriet-Iserentant, R. Vanleerberghe, and R. Vandenberghe, Phys. Status Solidi A **44**, 215 (1977).

[23] K. De Strooper, A. Govaert, C. Dauwe, and G. Robbrecht, Phys. Status Solidi A **37**, 127 (1976).

[24] J. Chen, X. Wu, and A. Selloni, Phys. Rev. B **83**, 245204 (2011).

[25] A. Lima, J. Phys. Chem. Solids **75**, 148 (2014).

[26] A. Lima, J. Phys. Chem. Solids **91**, 86 (2016).

[27] S. Selcuk and A. Selloni, J. Phys. Chem. C **119**, 9973 (2015).

[28] X. L. Xu, Z. H. Chen, Y. Li, W. K. Chen, and J. Q. Li, Surf. Sci. **603**, 653 (2009).

[29] P. Hohenberg and W. Kohn, Phys. Rev. **136**, B864 (1964).

[30] W. Kohn and L. J. Sham, Phys. Rev. **140**, A1133 (1965).

[31] G. Kresse and J. Furthmüller, Phys. Rev. B **54**, 11169 (1996).

[32] G. Kresse and J. Furthmüller, Comput. Mater. Sci. **6**, 15 (1996).

[33] G. Kresse and J. Hafner, Phys. Rev. B **47**, 558 (1993).

[34] P. E. Blöchl, Phys. Rev. B **50**, 17953 (1994).

[35] G. Kresse and D. Joubert, Phys. Rev. B **59**, 1758 (1999).

[36] J. P. Perdew, K. Burke, and M. Ernzerhof, Phys. Rev. Lett. **77**, 3865 (1996).

[37] J. Kuneš, I. Leonov, M. Kollar, K. Byczuk, V. I. Anisimov, and D. Vollhardt, Eur. Phys. JST **180**, 5 (2010).

[38] S. L. Dudarev, G. A. Botton, S. Y. Savrasov, C. J. Humphreys, and A. P. Sutton, Phys. Rev. B **57**, 1505 (1998).

[39] T. Roisnel and J. Rodríguez-Carvajal, WinPLOTR: A windows tool for powder diffraction patterns analysis, in *Proceedings of the Seventh European Powder Diffraction Conference (EPDIC 7)*, edited by R. Delhez and E. J. Mittenmeijer, Materials Science Forum (Scitec Publications, 2001), pp. 118–123.

[40] D. Das, R. Biswas, and S. Ghosh, J. Phys.: Condens. Matter **28**, 446001 (2016).

[41] G. L. Stamokostas and G. A. Fiete, Phys. Rev. B **97**, 085150 (2018).

[42] W. Roth, J. Phys. Chem. Solids **25**, 1 (1964).

[43] L. Khriplovich, E. Kholopov, and I. Paukov, J. Chem. Thermodyn. **14**, 207 (1982).

[44] V. Singh, M. Kosa, K. Majhi, and D. T. Major, J. Chem. Theory Comput. **11**, 64 (2014).

[45] S. Diaz, S. de Brion, G. Chouteau, B. Canals, V. Simonet, and P. Strobel, Phys. Rev. B **74**, 092404 (2006).

[46] S. Singh, P. Pramanik, S. Sangaraju, A. Mallick, L. Giebeler, and S. Thota, J. Appl. Phys. **121**, 194303 (2017).

[47] P. Kubelka and F. Munk, Z. Tech. Phys. **12**, 593 (1931).